Energy materials

Ionic liquid-assisted synthesis of tri-functional ruthenium oxide nanoplatelets for electrochemical energy applications

Sujoy Sarkar[1],* , Debdyuti Mukherjee[2], R. Harini[3], and G. Nagaraju[4]

[1] Chemistry Division, School of Advanced Sciences, Vellore Institute of Technology Chennai, Vandalur-Kelambakkam Road, Chennai, Tamil Nadu 600127, India

[2] Tandon School of Engineering, New York University, Brooklyn, NY 11201, USA

[3] Department of Electronics and Communication, Government Polytechnic, Tumakuru, Karnataka 572103, India

[4] Energy Materials Research Laboratory, Department of Chemistry, Siddaganga Institute of Technology, Tumakuru, Karnataka 572 103, India

ABSTRACT

Nanostructured crystalline metal oxides are in great demand in industrial processes due to their unique physicochemical properties and ionic liquids (ILs) are promising solvent for synthesizing such materials. Herein, we report an IL-assisted, facile, and environmental benign approach to synthesize rutile phase of ruthenium oxide (RuO_2) nanoplatelets (NPLs) structure with a size distribution of a few tens of nm. The key to this synthesis methodology is the use of imidazolium-based ILs as solvents and binder in the ionothermal process. The obtained RuO_2 phase is thoroughly characterized by spectroscopic and microscopic techniques. Further, the material is used as electrocatalyst toward electrochemical energy storage and conversion in an alkaline solution. The platelet morphology of RuO_2 exhibits excellent supercapacitor performance and its capacitance value is ~ 200 F g^{-1} in 1 M KOH solution. Besides, the as-synthesized RuO_2 NPLs shows superior water oxidation and chlorine evolution processes at a minimal overpotential, i.e., 1.47 V in 1 M KOH and 1.5 V in 3 M KCl (pH 3) electrolyte, respectively, exhibiting its tri-functional electrochemical behavior toward production of renewable energies. The present study demonstrates that single-step production of the NPL morphology of RuO_2 has potential implications in the field of electrolysis and supercapacitors.

Handling Editor: Christopher Blanford.

Address correspondence to E-mail: sujoy.sarkar@vit.ac.in

GRAPHICAL ABSTRACT
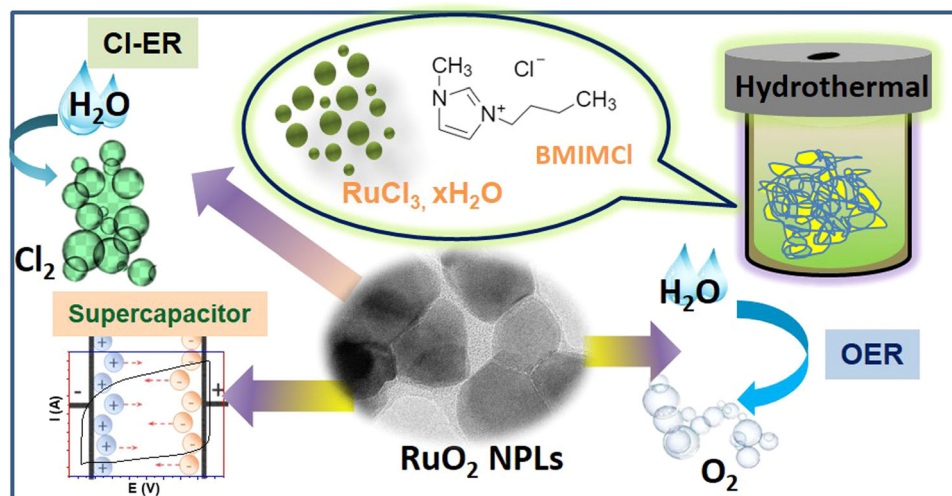
Introduction

Metals usually form a variety of oxide compounds and that oxide compounds are being applied in every aspect of energy storage and conversion, catalysis, sensor, data storage, medical and security, and so on because of their unique catalytic, electronic, magnetic, and optical properties [1–3]. In recent years, nanostructured crystalline metal oxides have drawn significant attention due to their interesting physicochemical properties and excellent performance in various energy-related applications [4]. Several novel strategies have been developed to obtain crystalline metal oxide nanoparticles and among them, the sol–gel method based on the hydrolysis and condensation of metal halides or metal alkoxides are extensively studied [5]; however, particle sizes in nanoregime and precise crystal morphologies are found to be challenging [6]. To overcome the challenge, room-temperature ILs, an environmentally benign solvent, have been introduced for synthesizing the inorganic nanomaterials. ILs usually possesses unique properties such as negligible vapor pressure, low inflammability, wide electrochemical windows, high inherent conductivities, thermal stability, liquidity over wide temperature ranges, and easy recycling that made this solvent more advantageous over

conventional solvents [7, 8]. ILs are basically organic salts made of only ions; moreover, it is a kind of non-conventional molten salts which can act as templates or effective solvents for many organic and inorganic synthesis with well-defined and extended ordering of nanoscale structures [9–12]. Particularly, imidazolium cation-based ILs are useful for many applications in synthetic chemistry and catalysis [13, 14] and act as suitable media for generation and stabilization of various nanomaterials. Therefore, different transition metal/metal oxide nanoparticles such as Au NPs, Co–Pt, ZnO, V_2O_5, and Mn_3O_4 with multiple shapes and sizes were prepared from room temperature ILs and reported elsewhere [15–20].

Among the different transition metal oxides, RuO_2 shows interesting properties such as low resistivity, high chemical, and thermodynamic stability [21]. It is considered to be a good electrocatalyst for different electrochemical energy storage like electrochemical supercapacitor material due to its wide potential window of facile redox reactions and high stability [22, 23]. This material is also treated as a well-known electrocatalyst for various electrochemical reactions such as water oxidation/reduction and chlorine evolution [24–27].

Due to the extensive industrial uses and potential applications, RuO_2 has been synthesized by different methods focusing on high yield at the low expenses.

Various synthetic protocols have been developed to synthesize RuO_2 such as sol–gel method, [28] and polyol method [29]. Among the different methods, hydrothermal methods are one of the attractive and easy methods to prepare metal oxide nanostructures at low temperature [30–32]. On the other hand, imidazolium-based IL was used as a template to fabricate the silica-supported RuO_2 nanoparticles [33]. Instead of using as template, ILs can be mixed with precursor materials and subjected to place in a hydrothermal autoclave for synthesizing the nanostructured crystalline materials [34, 35].

In the present study, imidazolium-based ILs-assisted hydrothermal method is employed to synthesize the nanostructured crystalline RuO_2 where 1-butyl-3-methylimidazolium chloride IL is used as size and shape controller of the nanoparticles as reported previously [35]. The crystallinity of the as-prepared RuO_2 was characterized using x-ray diffraction techniques while nanoplatelets (NPLs) morphology was investigated using FESEM and TEM. Later on, the material was used as an efficient electrocatalyst toward oxygen evolution reaction (OER) and chlorine evolution reaction (Cl-ER) in different mediums at different pH. The onset values for OER and Cl-ER were found to be 1.47 V in 1 M KOH and 1.5 V in 3 M KCl (pH 3) electrolyte, respectively. Apart from electrocatalysis, the charge storage capacity of this material was investigated in the alkaline medium. The capacity value was found to be ~ 200 F g^{-1} at a current density of ~ 1 A g^{-1}. It is noteworthy that no conducting materials or binders were mixed with as-synthesized material to improve the electrocatalytic activities. Hence, this method opens up a new method of synthesis NPLs rutile oxide structures for different electrochemical energy applications.

Experimental

Preparation of ruthenium (IV) oxide nanoplatelets

The material was prepared by IL-assisted hydrothermal method where 0.25 g of precursor (ruthenium chloride hydrate, $RuCl_3$, xH_2O, 99.9% Alfa Aesar) was mixed with 2.5 mL hydrogen peroxide and 30 mL water. Later, 0.5 g of 1-butyl-3-methylimidazolium chloride (BMIMCl, Sigma-

Aldrich, $\geq 98\%$) was added with constant stirring and transferred to a Teflon-lined autoclave. The mixture was subjected to heat treatment at 140 °C for 2 days. The autoclave was cooled to room temperature. The obtained product was washed with water and ethanol mixture (1:1). To remove excess ILs, the product was mixed with acetonitrile and stirred for overnight. The product was extracted from centrifugation (8,000 rpm for 30 min) and dried in an oven at 80 °C for overnight.

Physicochemical characterization

Powder X-ray diffraction data were recorded on Philips X'pert PRO X-ray diffractometer with graphite monochromatized Cu-K_{α} (1.5418 Å) radiation. The surface morphology of the product was examined by Carl Zeiss Ultra 55 FESEM operated at 10 kV accelerating voltage using in-lens detector equipped with energy-dispersive X-ray spectroscopy (EDS). TEM micrographs were recorded at JEOL JEM 1200 Ex operating at 200 kV. The TEM samples were prepared by drop coating the diluted dispersion on a carbon-coated copper grid and dried under vacuum for 12 h. Raman spectroscopy of the sample was recorded by LabRAM HR, Horiba Jobin Yvon (France) using a 514.5 nm air-cooled Ar^+ laser with $50\times$ long distance objective. X-ray photoelectron spectroscopic (XPS) analysis was performed on a Kratos Axis Ultra DLD X-ray photoelectron spectrometer with monochromatic Al K_{α} (1486.708 eV) radiation. The absorption spectrum of the sample was measured on a Perkin Elmer Lambda 750 UV–vis spectrometer.

All the electrochemical measurements were carried out on an electrochemical workstation (CHI 660C, CH Instruments, USA) using a conventional three-electrode setup. Electrochemical impedance spectroscopy (EIS) was conducted on Autolab electrochemical workstation (Metrohm). A glassy carbon electrode was used as a working electrode and a carbon rod was used as a counter electrode. The mercury/mercury oxide (MMO) and saturated calomel electrode (SCE) were used as the reference electrodes depending on the electrolytes. For electrochemical oxygen evolution, 1 M KOH solution was prepared from ultrapure water (Milli-Q, Millipore, ~ 18 mΩ cm) and used as an electrolyte, whereas for chlorine evolution reaction, 3 M aqueous NaCl solution (pH 3) was used as an electrolyte. In

both the cases, an electrolyte was purged with N_2 gas for 30 min prior to the experiment and N_2 atmosphere was maintained in the electrochemical cell. All potentials are calibrated with respect to a relative hydrogen electrode (RHE), where $E_{RHE} = E_{MMO-} + 0.97$ V; and $E_{RHE} = E_{SCE} + 0.27$ V, under the mentioned electrolyte condition. A 3-mm-diameter glassy carbon electrode was polished properly before the catalyst was drop casted. The catalyst ink was prepared in such a way that 2 mg catalyst powder was dissolved in 2 mL of isopropanol and water mixture (1:1) with the addition of 10 μL Nafion (5 wt% in aliphatic alcohol, Aldrich). Later, the mixture was ultrasonicated for 30 min and 10 μL ink was deposited on the polished glassy carbon electrode to obtain 140 μg cm^{-2} loading and dried under an ambient atmosphere.

Results and discussion

Physicochemical characterization

The structure of the as-prepared RuO_2 NPLs is investigated by powder XRD and the pattern is depicted in Fig. 1. The sharp diffraction peaks at 28.1°, 35.4°, and 54.6° are originated from (110), (011), and (121) planes of the rutile-type crystal structure of RuO_2. All other diffraction peaks are indexed accordingly. The obtained pattern is compared with

standard XRD data (ICSD # 84618) and found that experimental data (black) is well matched with the standard tetragonal RuO_2 (red bar). The crystallite size of the sample is determined using the Scherrer formula [36] [$D = K\lambda/\beta \cos\theta$, where λ is the wavelength of the X-ray beam, θ is diffraction angle, D is the crystallite size, K is shape factor, and β is full-width half maximum (FWHM) of the peak] from the FWHM of (110) peak ($2\theta = 28.25°$). The calculated value, 40 nm, is in agreement with those estimated by microscopy. The dislocation density (δ) of the RuO_2 NPLs was calculated using $\delta = 1/D^2$ equation, where D is the crystallite size obtained from XRD [37] and the value is found to be 5.4×10^{-4} nm^{-2}. It represents the amount of defects present in the sample, i.e., the length of dislocation per unit volume of the crystal and it is noteworthy that the value of dislocation density for a perfect crystal is close to zero.

Crystal structure of rutile RuO_2 is drawn using the X'Pert Highscore software where the structure is projected along [001] direction and structure is viewed along the 'c' axis. RuO_2 belongs to the space group D_{4h}^{14} and possesses tetragonal rutile crystal structure and it contains two RuO_2 molecules per unit cell as shown in Fig. 1b. It is found that the Ru^{4+} is located at sites with D_{2h} symmetry and O^{2-} occupies the sites with C_{2v} symmetry. In a unit cell, cations are bounded by six anions at the corners of a slightly distorted octahedron.

Figure 1 **a** X-ray diffraction patterns of rutile RuO_2 NPLs (black) and standard ICSD data (File No. 84618) (red). **b** Crystal structure of rutile RuO_2 along the [001] projection (view along the 'c' axis). **c** and **d** FESEM images of RuO_2 NPLs at different magnifications.
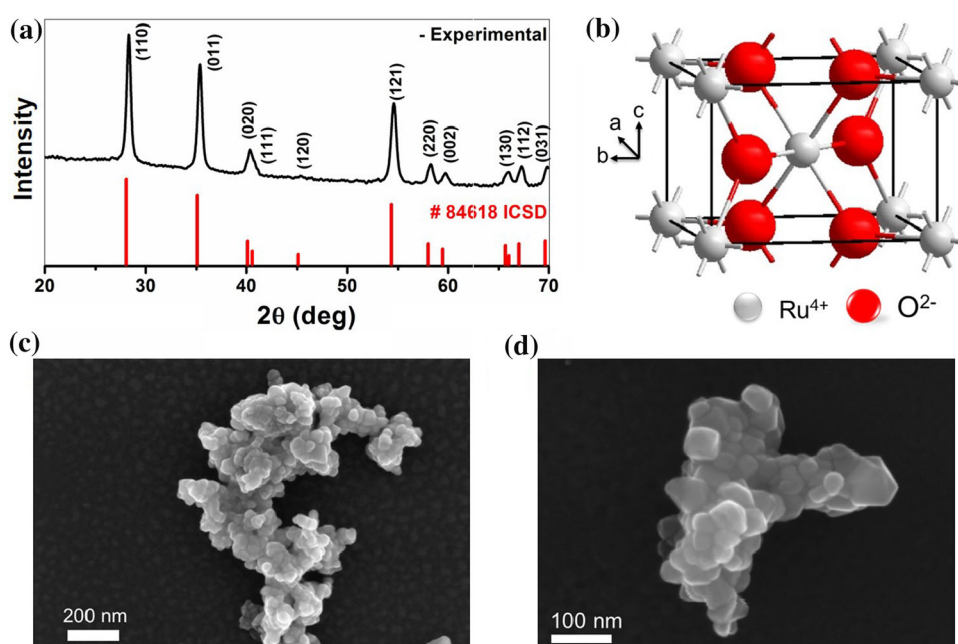
The morphology of the as-synthesized RuO$_2$ NPLs is examined using field emission SEM (FESEM) and depicted in Fig. 1c and d. In the lower magnification of the image (Fig. 1c), the platelets like morphology are found to be agglomerated, whereas at higher magnification (Fig. 1d), the platelet structures are clear with average size 20–100 nm. To ensure the components present in the RuO$_2$ NPLs, EDS along with elemental mapping is carried out (Fig. S1a) and found the sharp signal of Ru and O in the EDS spectrum. Further, the Ru and O signals found in the elemental mapping are well matched with SE2 micrograph (Fig. S1b).

To understand the morphology and structure of RuO$_2$ NPLs more precisely, the sample is further investigated by TEM (Fig. 2). The platelet shape of RuO$_2$ is clearly extracted from the bright-field TEM images (Fig. 2a). The darker patches appeared in the micrographs are due to the overlaid of the nanoplatelets and it is further deciphered from the higher magnification image (Fig. 2b). The average particle size (40 nm) of the RuO$_2$ NPLs is found to be similar to the crystallite size of the RuO$_2$ (inset Fig. 2c).

The ploycrystallinity nature of the RuO$_2$ NPLs is evaluated from the SAED pattern shown in Fig. 2c. The pattern contains the characteristic ring pattern with a few bright spots, where each spot is attributed to the Bragg reflection of an individual crystallite.

The obtained rings are relatively continuous, which reveals that the crystallites are small and in a random orientation. The high-resolution TEM (HRTEM) image in Fig. 2d exhibits that a few platelets are oriented in the (110) direction and the attached neighboring particle is oriented in the (011) direction. The distance between lattice planes is measured (shown in inset Fig. 2d) from the HRTEM image and the values are found to be 3.1 Å and 2.5 Å for d$_{110}$ and d$_{011}$, respectively, which are in good agreement with the cell parameters of RuO$_2$ (cell parameters $a = 4.544$ Å, $c = 3.140$ Å) [38].

To understand the shape of the nanocrystals, a plausible mechanism of RuO$_2$ NPLs prepared by ILs-assisted process is illustrated in Scheme 1. Firstly, Ru(III)Cl$_3$ is reacted inside the autoclave and formed Ru-hydroxide [Ru(OH)$_3$], which is subsequently converted into RuO$_2$ nanoparticles in the presence of H$_2$O$_2$ [39]. The shape of nanocrystals is determined by the tendency to form aggregates of the initial seeds while minimizing the surface energies. In the subsequent self-assembled process, BMIMCl plays a crucial role on the shape of the RuO$_2$ nanocrystals. Imidazolium-based ILs have a polymeric supramolecular structure consisting of anionic and cationic aggregates, which can form two-dimensional polymeric self-assemblies as shown in the Scheme 1. The imidazolium cation could be selectively

Figure 2 TEM images of RuO$_2$ NPLs at **a** lower magnifications and **b** higher magnifications along with **c** SAED pattern (inset shows particle distribution curve) and **d** HRTEM image (inset shows the d-spacing).
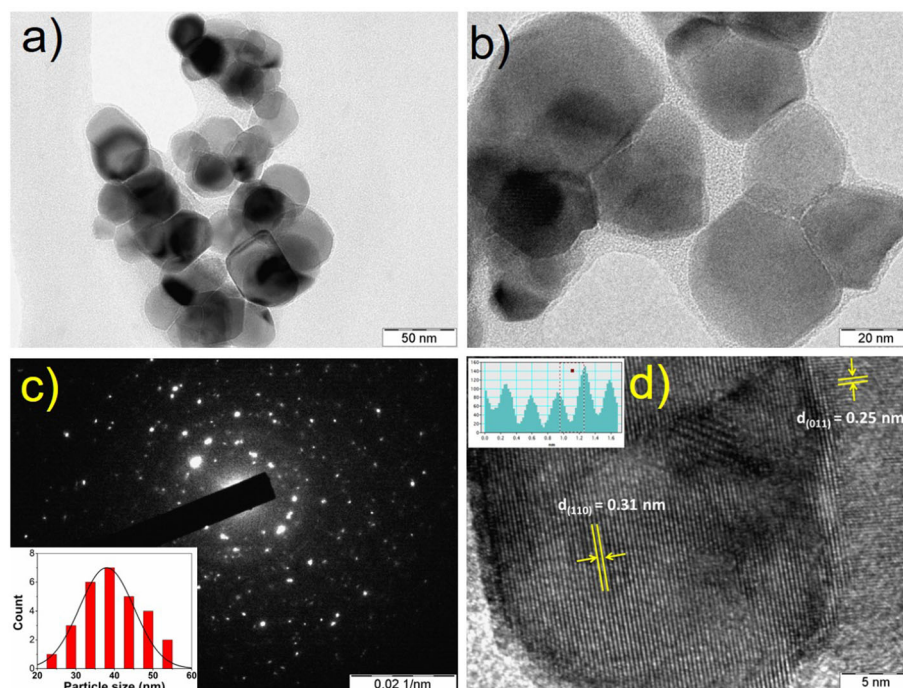
Scheme 1 Schematic illustration of synthesis of ILs-assisted RuO$_2$ NPLs.
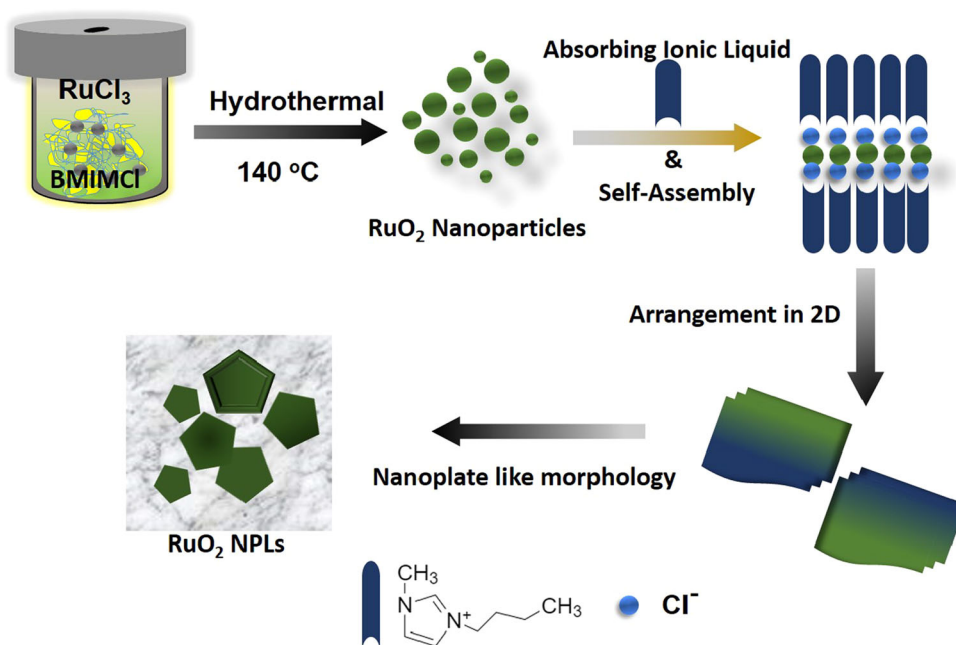
adsorbed on the particular crystal plane [e.g., (110) planes of RuO$_2$], where charges can be counterbalanced due to the electrostatic forces between O^{2-} termination of RuO$_2$ and (BMIM)$^+$ of ILs. Hence, the ILs act as a template on the formation of the building blocks of the nanoplatelet. On the other hand, Cl$^-$ ion can adsorb on the RuO$_2$ nanoparticles, followed by alignment of imidazolium cation, which subsequently provide special interlayer spaces for the arrangement of RuO$_2$ nanoparticles in the 2D directions. Hence, the ILs form a protective layer, composed of supramolecular anionic aggregates, which surrounds the RuO$_2$ nanoplate surfaces in a constructive way and provides both steric and electronic protection to the nanoparticles against aggression. Apart from electrostatic interaction, hydrogen bonding and π–π stacking results in realignment of the building blocks toward a specific direction with the minimization of the surface energy and appear as a platelet structure of RuO$_2$ via aggregation and organization [40]. Hence, it can be anticipated that selective adsorption of ILs on RuO$_2$ crystal planes can change its atomic arrangement or surface termination, as a result the growth process is affected and well-defined nanoplates are formed.

XPS characterization is performed to investigate the chemical state variation of the elements present in the as-synthesized RuO$_2$ NPLs. The survey XPS spectrum which contains all the elements present in RuO$_2$ NPLs is shown in Fig. 3a. Ruthenium is

typically analyzed in XPS by considering the strong signals from the 3d photoelectrons. To understand further, Ru 3d spectrum is deconvoluted into four peaks, which were identified with Ru 3d$_{5/2}$ and Ru 3d$_{3/2}$ appeared at 281.5 and 285.7 eV, respectively. It is observed that Ru 3d$_{5/2}$ peak did not overlap with Ru 3d$_{3/2}$ and C 1s peaks and the binding energy of Ru^{4+} corresponds to the Ru 3d$_{5/2}$, suggesting the presence of RuO$_2$. Apart from, two small intensity peaks were observed at 283.5 and 287.7 eV corresponding to the Ru 3d$_{5/2}$ and Ru 3d$_{3/2}$, respectively [41], which could be related to the presence of a small fraction of RuO$_3$.

The interference of C 1s signal often overlaps with Ru 3d signal and it is observed in Fig. 3a where a peak appeared at 285.0 eV is labeled for typical C 1s (–C–H) which is also used for binding energy calibration. Apart from, 285.0 eV peak, two more peaks are observed in the higher binding energy in the same spectra such as 287.0 and 289.0 eV could be labeled as –C–O and –C=O, respectively.

Additionally, deconvoluted and well-fitted XPS O1s also confirmed the existence of RuO$_2$ and the oxygen-containing functional groups were identified with Ru–O–Ru, (529.4 eV), –C–O (530.6 eV), and C–OH (534.5 eV). The peak centered at 530.6 eV could be due to the Ru–OH. The presence of oxygen-containing functional groups could be present due to the IL used during the synthesis which would improve

Figure 3 a Survey XPS spectrum of RuO$_2$ NPLs; **b** high resolution and deconvoluted Ru 3d and **c** O 1s; **d** Raman spectrum of RuO$_2$ NPLs.
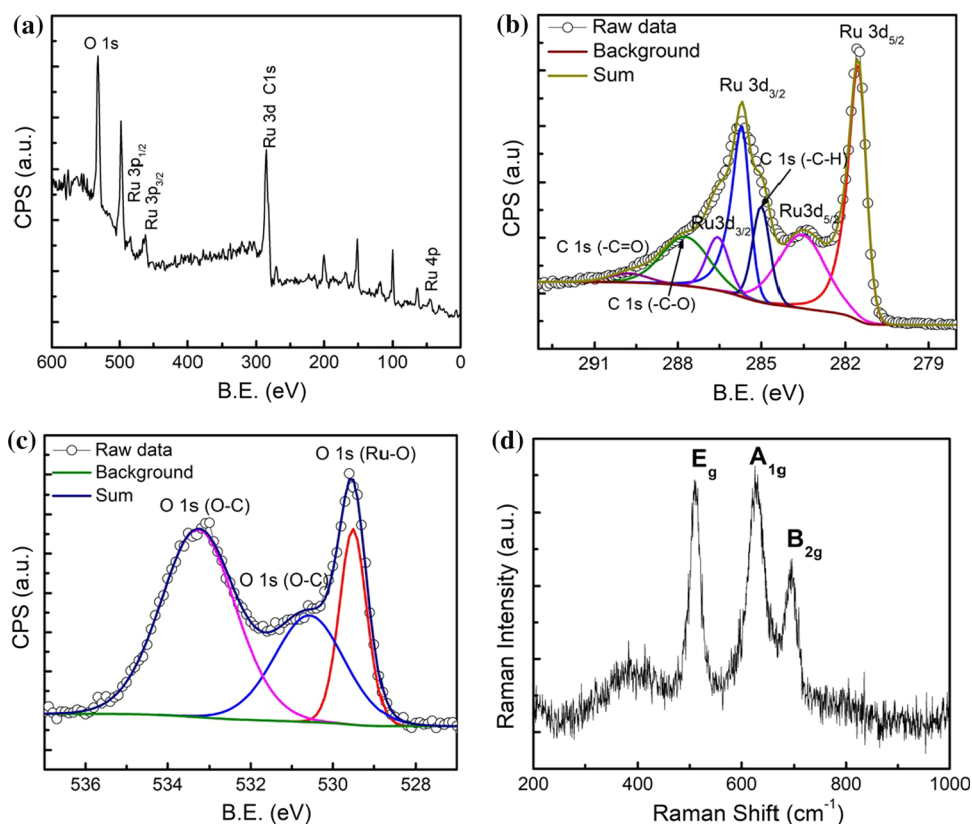
the electrical conductivity and electrochemical stability of the as-synthesized RuO$_2$ NPLs.

According to the group theory, fifteen optical phonon modes are possible and among them, only three modes are Raman active. The Raman spectrum of RuO$_2$ NPLs is shown in Fig. 3d where three major Raman features, namely E$_g$, A$_{1g}$, and B$_{2g}$ modes, centered at 511, 628, and 694 cm^{-1}. The full-width half maxima of the peaks are found to be higher for RuO$_2$ NPLs than for the single crystal RuO$_2$ [42, 43] implying the polycrystalline nature of the RuO$_2$ as confirmed from the XRD and TEM studies.

## Electrochemical energy storage

The electrochemical performance of the RuO$_2$ NPLs as an electrode material for supercapacitor is examined in a conventional three-electrode system using cyclic voltammograms (CVs) in deaerated 1 M KOH solution. The steady-state voltammograms show a typical capacitive behavior of the as-synthesized RuO$_2$ NPLs measured as a function of the potential scan rates (Fig. 4a). In order to evaluate the high-rate capability of RuO$_2$ NPLs in the assigned potential window, the scan rate is varied from 0.01 to 0.5 V s^{-1}.

The practical potential window is fixed for capacitance studies from 0.2 to 0.95 V vs. RHE. The rectangular shape of the voltammograms remains symmetrical in different scan rates implying the insignificant iR loss with the scan rate variation [44]; moreover, electrochemical processes occurred at the interface are highly reversible [45].

The specific capacitance, more preciously, volumetric capacitance is found to be decreased with increasing potential scan rates, depicted in Fig. 4b. The volumetric capacitance is calculated using the formula, $C_{sp} = \int i \, dV/(v \cdot A \cdot \Delta V)$, where $\int i \, dV$ implies to the area under the CV curve, v is the potential scan rate, A is the geometric area of the electrode and $\Delta V = (V_{max} - V_{min})$, V_{max} is the potential at the end of charge and V_{min} at the end of discharge. The capacitance of the RuO$_2$ NPLs at 0.01 V s^{-1} scan rate is determined to be 22.3 mF cm^{-2}.

The electrochemical capacitance behavior of the RuO$_2$ NPLs is further evaluated by galvanostatic charge–discharge techniques (GCD) under the applied current densities varying from 0.8, 1.6, and 3.2 A g^{-1}. The capacitive behavior of the RuO$_2$ NPLs is observed from the linear V–t plots in Fig. 5a. The specific capacitance is determined using the equation,

Figure 4 a Cyclic voltammograms of RuO_2 NPLs recorded at different scan rates by using 1 M KOH as electrolyte. **b** Specific capacitance as a function of potential scan rates.
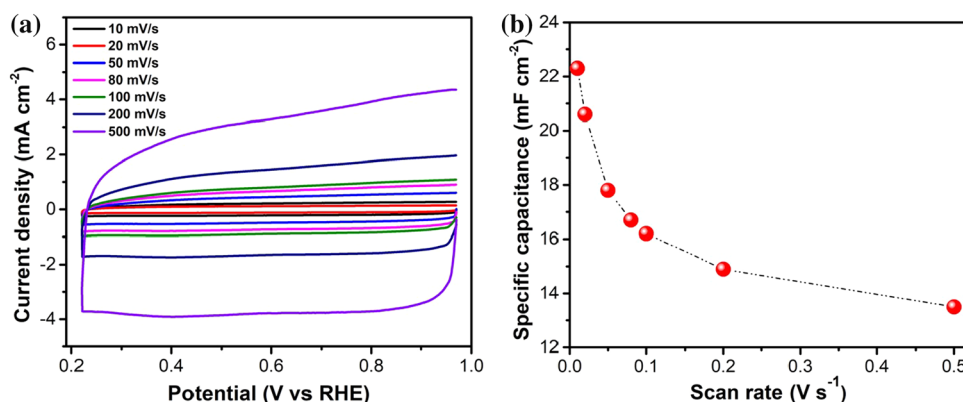
Figure 5 a Galvanostatic charge–discharge curve of RuO_2 NPLs at different current densities; **b** rate capability of RuO_2 NPLs; inset shows the Ragone plot of RuO_2 NPLs-based supercapacitors; **c** cycling stability (inset) and capacity retention of RuO_2 NPLs-based supercapacitor; **d** potentiostatic electrochemical impedance spectroscopy (EIS) measurements conducted between 100 mHz and 1 MHz with an amplitude of 5 mV; inset shows the Bode plot.
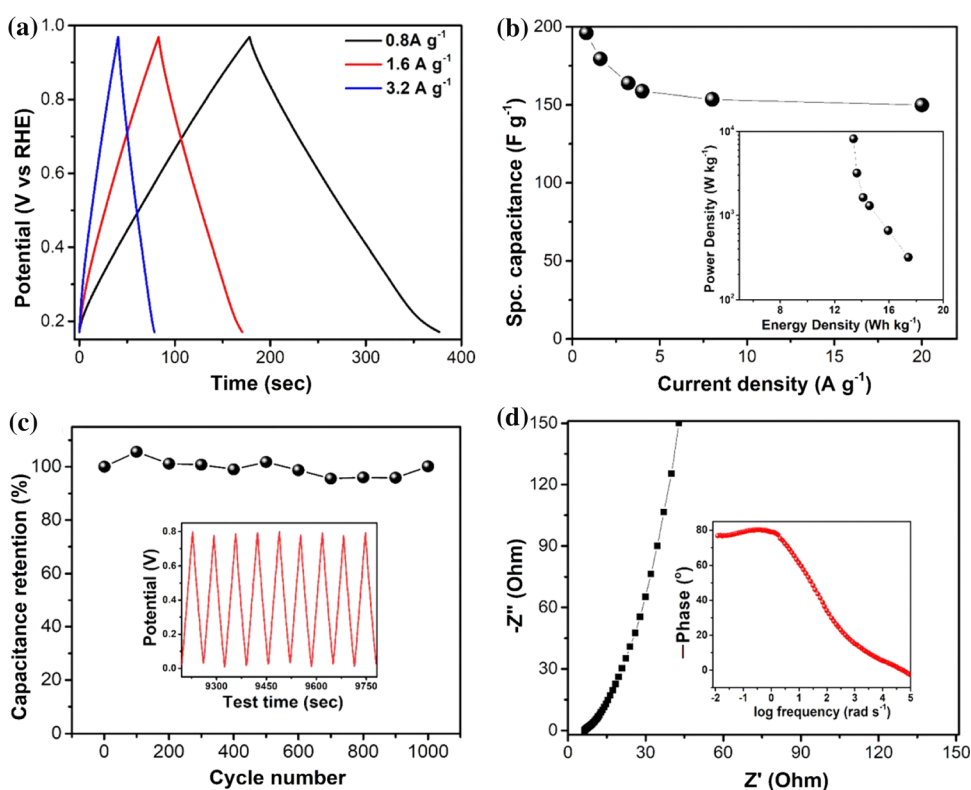
$$C_{sp} = I \, \Delta t/m \cdot \Delta V,$$

where I is the specific discharge current, Δt is the discharge time, m is the mass of the electroactive material, and ΔV is the applied potential window. By using this equation, specific capacitance is measured at different discharge current. Figure 5b shows the specific capacitance variation with the discharge current densities in the range of 0.8 A g^{-1} to 20 A g^{-1} in the aqueous electrolyte and the capacitance values are decreased with increasing the current densities. The specific capacitances of the RuO_2 NPLs in the alkaline solution are 198.2 F g^{-1} and 150.7 F g^{-1} at

current densities of 0.8 A g^{-1} and 20 A g^{-1}, respectively. The origin of the capacitance can be explained from double-layer capacitance along with additional faradic capacitance where Ru^{4+}/Ru^{3+} redox couple shuttles at the outermost layer of RuO_2 aggregates.

Moreover, ultrathin nanoplatelets of as-synthesized RuO_2 are connected well with each other (assessed from the TEM image), possibly enhanced by the presence of IL during the formation indirectly helps the fast charge transport between the electrode surface and RuO_2 surface. The capacitance values of RuO_2 NPLs obtained from the present study are higher than reported RuO_2 nanoparticles and

comparable to the carbon-based RuO_2 composites [46, 47] as shown in Table S1.

The Ragone plot, power density vs. energy density, is one of the important assessable parameters used for electrochemical performance comparison of various energy storage devices, especially supercapacitors and batteries. The energy (E) and power (P) densities are calculated from the GCD curves by using the equations, $E = C_{sp}(\Delta V)^2/2 \times 3600$ and $P = E/t$, where C_{sp} is the specific capacitance, ΔV is the potential range, and t is the discharge time in hour unit. Inset of Fig. 5b illustrates the Ragone plot of RuO_2 NPLs in the alkaline solution. The maximum energy density of RuO_2 NPLs is found to be 17.4 Wh kg^{-1} in 1 M KOH solution, which is higher than the reported RuO_2 nanoparticles [29]; is achieved at the current density of 0.8 A g^{-1}. However, the maximum power density of 8.2 kW kg^{-1} is obtained for the same material, indicating that nanoplatelet morphology of the as-synthesized RuO_2 NPLs would be a promising material for high power electrochemical energy devices.

The cyclic performance is another crucial factor for the electrochemical devices implementing in practical use, is examined by chronopotentiometry at a current density of 4 A g^{-1} in the potential range 0.17 V to 0.97 V vs RHE. As seen in Fig. 5c, the cycling stability of the RuO_2 NPLs in 1 M KOH solution is slightly decreased and the capacitance retentions after 1000 cycles run are found to be 94.6%, implying good electrochemical stability. Further shown in the inset of Fig. 5c, the GCD curve shape at a certain test time is symmetrical, indicating the stability of the RuO_2 NPLs during cycling performance.

The supercapacitive nature of the as-synthesized RuO_2 NPLs is further explored by EIS, which was carried out in the broad frequency range of 100 kHz to 10 mHz at a small sine wave amplitude of 5 mV. The Nyquist plot in Fig. 5d exhibits a typical semicircle over the high-frequency range and a vertical line in the low-frequency region. EIS is carried out to further characterize the capacitor behavior. The AC impedance is measured in the frequency range from 100 kHz to 10 mHz. The straight line nearly parallel to the imaginary axis shows ideal capacitive behavior of the material, consistent with the finding from CV and GCD studies. The intercept of the Nyquist plot on the real axis is about $\sim 6\ \Omega$, showing good conductivity of the electrolyte and very low internal resistance of the electrode caused by the mobility of ions in the electrode–electrolyte interface. The Bode plot (phase angle vs frequency) of the RuO_2 NPLs is depicted in the inset of Fig. 5d where the phase shift is $\sim 80°$ in the low-frequency region indicating the double layer charge storage behavior and hardly found any faradic charge storage phenomena of the RuO_2 NPLs [48].

Electrocatalytic oxygen evolution reaction

The electrocatalytic activity of RuO_2 NPLs toward evolution of oxygen is investigated in a conventional three-electrode setup where the catalyst coated on glassy carbon electrode is used as a working electrode in 1 M KOH solution. The iR corrected liner sweep voltammogram of RuO_2 NPLs is compared with bare GC and commercial RuO_2 with similar mass loading, recorded at 5 mV s^{-1} scan rate, and depicted in Fig. 6a. As observed from the LSVs, the bare GC electrode is used as control measurement for the OER, hardly contributes to the electrocatalytic activity with minimal current density. RuO_2 NPLs shows the OER onset overpotential as low as $\eta = 240$ mV (~ 1.47 V vs RHE), which is better than the standard RuO_2 (~ 1.53 V vs RHE). The overpotential, required to achieve 10 mA cm^{-2} current density, normally regarded as equivalent to solar fuel synthesis, is $\eta = 400$ mV (~ 1.63 V vs. RHE), very close to the best-reported catalyst so far [49] and a few millivolt less than commercial RuO_2 as shown in Fig. 6a. The low onset overpotential and high current density indicate the excellent OER performance of RuO_2 NPLs in alkaline solution.

To achieve more insight into the oxygen evolution process of RuO_2 NPLs, electrocatalytic kinetics is further evaluated using Tafel plot (η vs log i), derived from the polarization curves as shown in Fig. 6b. The liner region of the Tafel plot is recorded at low and high overpotentials to obtain the Tafel slopes using the Tafel equation: $\eta = a + b \log i$, where b is the Tafel slope and i is the current density. Due to the change in the rate-limiting step, two different Tafel slopes can be deduced from the Tafel plot (Fig. 6b), that are, 82.5 mV dec^{-1} in low potential range and 132.4 mV dec^{-1} in the high potential range. Two Tafel slopes have been recognized for the oxygen evolution process. Moreover, it is reported that at high overpotential region (~ 1.4 V), crystalline RuO_2 films show the Tafel slopes in the region of 60 mV dec^{-1}, whereas at large current densities it is 120 mV dec^{-1}

Figure 6 **a** LSVs for oxygen evolution reaction on RuO_2 NPLs in 1 M KOH solution (pH ∼ 13); Scan rate was 5 mV s^{-1}. Inset shows the zoomed area near the onset region; **b** Tafel slope for the RuO_2 NPLs; **c** cycling stability of RuO_2 NPLs in 1 M KOH solution; LSVs of before and after cycling; **d** Amperometric i–t curve at 1.6 V for 5.5 h.
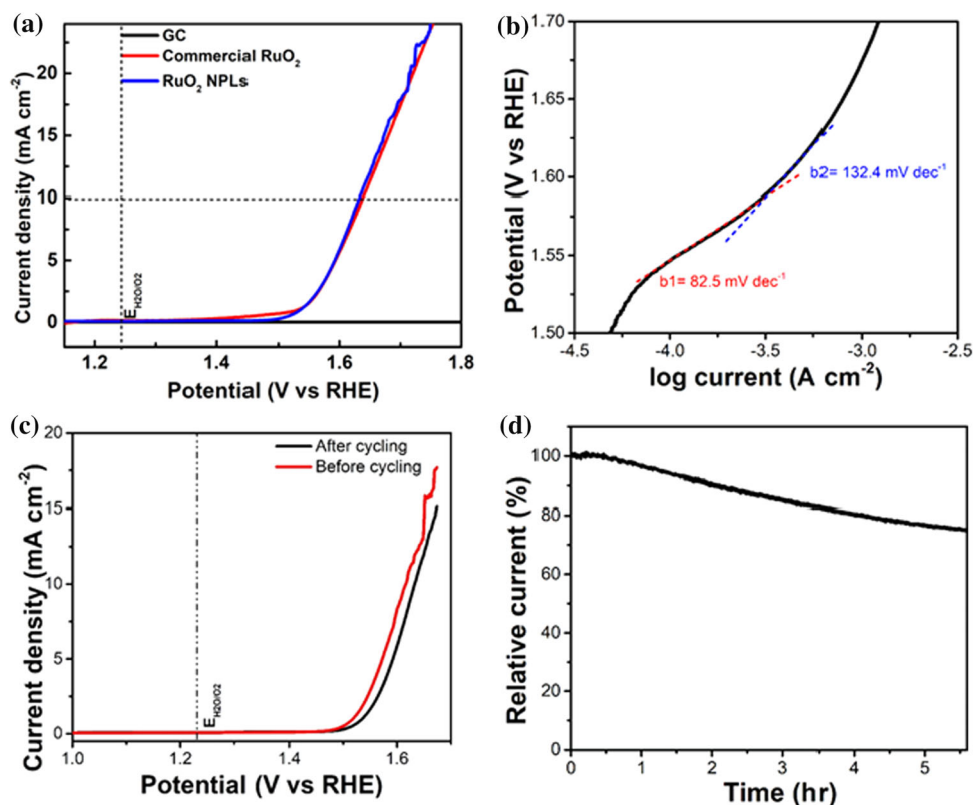
[50]. The better electrocatalytic performance of the RuO_2 NPLs toward OER can be explained by the presence of non-stoichiometric RuO_x which provides the active sites to adsorb the hydroxyl radicals from alkaline water.

The electrochemical durability of an OER electrocatalyst is one of the prime concerns for a practical implication. Therefore, a chronoamperometric durability test is performed to evaluate the long-term stability of RuO_2 NPLs in an alkaline solution. Figure 6c shows the comparison between the linear sweep voltammograms, performed before and after the chronoamperometric durability rest, revealing the stability of the electrode material by changing a minute change in the onset overpotentials. Further, Fig. 6d reveals that the RuO_2 NPLs retains almost 80% initial current at 1.6 V vs RHE after 5.6 h continues running in 1 M KOH solution.

Electrocatalytic chlorine evolution reaction

The catalytic activity of the present catalyst has also been studied for electrochemical chlorine evolution reaction (Cl-ER) using conventional three electrodes system using the RuO_2 NPLs coated on GC as working electrode, Pt and SCE as counter and reference electrode, respectively. The electrolyte that was used for this experiment is deaerated 3 M NaCl solution at pH 3. Figure 7a represents the iR corrected LSV drawn at 5 mV s^{-1} scan rate that indicates excellent Cl-ER efficiency with an onset potential 1.5 V. The Cl-ER activity of RuO_2 NPLs was further compared with the commercial RuO_2 and depicted in Fig S2a, which shows that both catalysts possess the same inflection point (∼ 1.5 V); however, at higher current density (15 mA cm^{-2} or more), RuO_2 NPLs exhibits lower overpotential than the commercial one.

Further, the Tafel polarization measurement (inset of Fig. 7a) exhibits lower Tafel slope (42 mV dec^{-1}) for the RuO_2 NPLs. The Tafel slope for Cl-ER was found to be around 35 to 40 mV dec^{-1} for the standard DSA electrocatalyst [51]. This result suggests that Cl-ER follows the Volmer–Heyrovsky mechanism as proposed earlier [52, 53].

It is noteworthy that the thermodynamic potentials for chlorine evolution (Cl-ER) and oxygen evolution (OER) are close to each other (1.36 V for Cl-ER and 1.23 V for OER) [51]; moreover, RuO_2 nanoparticles are known to be a good OER catalyst in the acidic
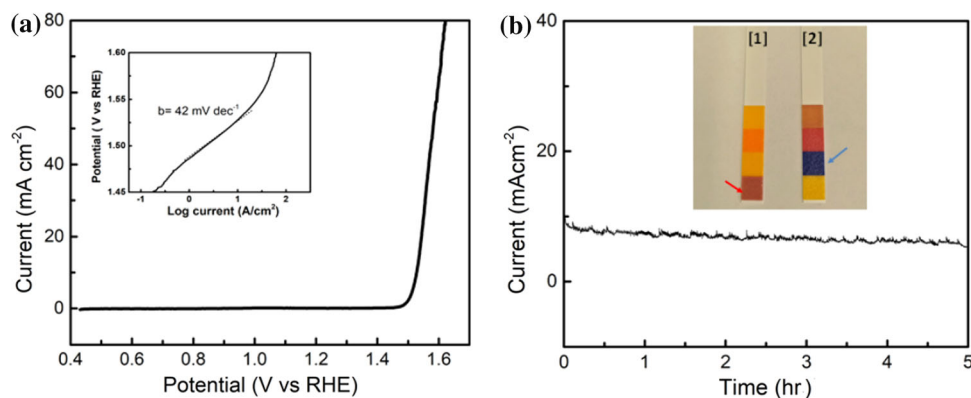
Figure 7 **a** LSV for the RuO_2 NPLs as a catalyst in 3 M NaCl (pH 3). Scan rate: 5 mV s^{-1}. Inset shows the Tafel slope for chlorine evolution from the same electrolyte. **b** Amperometric *i*–*t* was performed for RuO_2 NPLs at a constant potential of 1.5 V for 5 h; inset shows the pH indicator papers: (1) before Cl_2 evolution, (2) after Cl_2 evolution; arrows indicate the color change occurred due to the change in solution pH.

medium due to the sequential water dissociation on oxide surface [54]. Hence, there is always a possibility of interference of OER during Cl-ER and it is important to confirm the actual phenomena. Therefore, the chlorine evolution was proved by using both litmus test (Inset of Fig. 7b) and bleaching test (Supporting Information, Movie) where the litmus test confirms that solution pH has increased from acidic to basic by following an equation [NaCl + H$_2$O → Cl$_2$ + H$_2$ + NaOH] as shown in Fig. 7b (inset). The arrow indicates that red color of the pH indicator paper (MColorpHast universal pH indicator, Germany) was turned into blue (blue arrow) due to the formation of NaOH during the chlorine evolution and solution pH is increased from acidic to alkaline.

In the second test, we have shown that huge chlorine gas is evolved from the electrode surface and during the gas evolution, a pH indicator paper was inserted into the electrochemical cell. It is observed that within a few seconds, the color of the paper is completely bleached (Supporting Information, Movie). These two experiments confirm that RuO_2 NPLs act as good electrocatalyst for Cl-ER in NaCl solution. To evaluate the selectivity of the RuO_2 NPLs electrode between the Cl-ER and OER, LSV curves were acquired in 3 M NaCl and 3 M NaNO$_3$ (~ pH 3) solutions, respectively. As shown in Fig. S2b, the curve recorded in non-chloride (NaNO$_3$) solution has higher onset potential than chloride solution during the positive potential scan, which could be due to the oxygen evolution. This result indicates the high selectivity of RuO_2 NPLs toward Cl-ER.

Long-term stability of the electrocatalysts is one of the concerns in any electrocatalytic reaction. The rutile structures are active materials for Cl_2 production; however, RuO_2 is relatively unstable at high overpotential and long run due to formation of corrosive species like HClO. Therefore, RuO_2 is mixed with IrO_2 and supported by TiO_2/SnO_2, known as dimensionally stable anodes (DSA) [55] is commonly used for large-scale Cl_2 production. For that, RuO_2 NPLs is kept at a fixed potential (1.5 V) for five long hours and hardly any change in the current density is observed, implying that ILs-assisted RuO_2 NPLs improve the stability of the material. Hence, it has been shown that RuO_2 prepared by IL-assisted method is found to be comparable with different RuO_2 nanostructures and their composites. The comparative electrocatalytic activities and supercapacitor performance are tabulated in Table S1 (Supporting Information) exhibiting tri-functional behavior of RuO_2 NPLs.

Conclusions

A simple, single-step, and low-temperature ILs-assisted method was employed for synthesizing RuO_2 nanoplatelets for tri-functional electrochemical energy applications. The physicochemical characterizations were carried out by XRD, XPS, SEM, and TEM analyses, revealing the nanoplatelet shape with high crystallinity. It is noteworthy that the material was synthesized without addition of any surfactant or binder, only IL played a key role in the formation

of the anisotropic structure of RuO$_2$. The electrochemical activities such as electrocatalysis and supercapacitor were investigated using as-synthesized RuO$_2$ NPLs and found that the RuO$_2$ NPLs can store a huge charge by showing a capacitance value of ~ 200 F g^{-1}. Similarly, the electrocatalytic parameters such as onset potential, Tafel slope, and electrochemical stabilities are up to the mark for the as-synthesized RuO$_2$ NPLs for both chlorine and OERs. Hence, ILs-assisted method opens a new pave for synthesis of the nanostructured, anisotropic, platelet shape of metal oxides, which could be used as useful electrocatalyst for energy storage and conversion in the present energy crisis situation.

Acknowledgements

Funding

Declarations

Conflict of interest The authors declare that they have no conflict of interest.

Supplementary Information: The online version contains supplementary material available at http s://doi.org/10.1007/s10853-022-07120-z.

References

[1] Noguera C (1996) Physics and chemistry at oxide surfaces. Cambridge University Press, Cambridge

[2] Diwald O, Berger T (2021) Metal oxide nanoparticles: formation, functional properties, and interfaces, 2. Wiley, Hoboken

[3] Nunes D, Pimentel A, Santos L, Barquinha P, Pereira L, Fortunato E, Martins R, Korotcenkov G (2018) Metal oxide nanostructures: synthesis, properties and applications. Elsevier Science, Oxford

[4] Chavali MS, Nikolova MP (2019) Metal oxide nanoparticles and their applications in nanotechnology. SN Applied Sciences 1:607

[5] Niederberger M (2007) Nonaqueous sol–gel routes to metal oxide nanoparticles. Acc Chem Res 40:793–800

[6] Niederberger M, Garnweitner G, Pinna N, Neri G (2005) Non-aqueous routes to crystalline metal oxide nanoparticles: Formation mechanisms and applications. Prog Solid State Chem 33:59–70

[7] Welton T (1999) Room-temperature ionic liquids. Solvents for synthesis and catalysis. Chem Rev 99:2071–2084

[8] Hallett JP, Welton T (2011) Room-temperature ionic liquids: solvents for synthesis and catalysis. 2. Chem Rev 111:3508–3576

[9] Ma Z, Yu J, Dai S (2010) Preparation of inorganic materials using ionic liquids. Adv Mater 22:261–285

[10] Dupont J, de Souza RF, Suarez PAZ (2002) Ionic liquid (molten salt) phase organometallic catalysis. Chem Rev 102:3667–3692

[11] Zhang T, Doert T, Wang H, Zhang S, Ruck M (2021) Inorganic synthesis based on reactions of ionic liquids and deep eutectic solvents. Angew Chem Int Ed 60:22148–22165

[12] Yu G, Mu M, Li J, Wu B, Xu R, Liu N, Chen B, Dai C (2020) Imidazolium-based ionic liquids introduced into π-electron donors: highly efficient toluene capture. ACS Sustain Chem Eng 8:9058–9069

[13] Dupont J, Scholten JD (2010) On the structural and surface properties of transition-metal nanoparticles in ionic liquids. Chem Soc Rev 39:1780–1804

[14] Valkenberg MH, deCastro C, Hölderich WF (2002) Immobilisation of ionic liquids on solid supports. Green Chem 4:88–93

[15] Oliveira FCC, Effenberger FB, Sousa MH, Jardim RF, Kiyohara PK, Dupont J, Rubim JC, Rossi LM (2011) Ionic liquids as recycling solvents for the synthesis of magnetic nanoparticles. Phys Chem Chem Phys 13:13558–13564

[16] Wang Y, Yang H (2005) Synthesis of CoPt nanorods in ionic liquids. J Am Chem Soc 127:5316–5317

[17] Zou H, Luan Y, Ge J, Wang Y, Zhuang G, Li R, Li Z (2011) Hierarchical Bi$_2$O$_2$CO$_3$ microspheres with improved visible-light-driven photocatalytic activity. CrystEngComm 13:2656–2660

[18] Kaper H, Willinger M-G, Djerdj I, Gross S, Antonietti M, Smarsly BM (2008) IL-assisted synthesis of V$_2$O$_5$ nanocomposites and VO$_2$ nanosheets. J Mater Chem 18:5761–5769

[19] Bussamara R, Melo WWM, Scholten JD, Migowski P, Marin G, Zapata MJM, Machado G, Teixeira SR, Novak MA,

Dupont J (2013) Controlled synthesis of Mn_3On nanoparticles in ionic liquids. Dalton Trans 42:14473–14479

[20] Jia H, Zhou H (2016) Synthesis of micronsized gold nanoplates at low precursor concentration using ionic liquid as novel subphase solvent. Int J Chem Eng Appl 7:173–177

[21] Ko D-S, Lee W-J, Sul S, Jung C, Yun D-J, Kim H-G, Son W-J, Chung JG, Jung DW, Kim SY, Kim J, Lee W, Kwak C, Shin JK, Kim J-H, Roh JW (2018) Understanding the structural, electrical, and optical properties of monolayer h-phase RuO_2 nanosheets: a combined experimental and computational study. NPG Asia Mater 10:266–276

[22] Xia H, Shirley Meng Y, Yuan G, Cui C, Lu L (2012) A symmetric RuO_2/RuO_2 supercapacitor operating at 1.6 V by using a neutral aqueous electrolyte. Electrochem. Solid State Lett 15:60

[23] Hu C-C, Chang K-H, Lin M-C, Wu Y-T (2006) Design and tailoring of the nanotubular arrayed architecture of hydrous RuO_2 for next generation supercapacitors. Nano Lett 6:2690–2695

[24] Galani SM, Mondal A, Srivastava DN, Panda AB (2020) Development of RuO_2/CeO_2 heterostructure as an efficient OER electrocatalyst for alkaline water splitting. Int J Hydrogen Energy 45:18635–18644

[25] Gao X, Chen J, Sun X, Wu B, Li B, Ning Z, Li J, Wang N (2020) Ru/RuO_2 Nanoparticle composites with N-doped reduced graphene oxide as electrocatalysts for hydrogen and oxygen evolution. ACS Appl Nano Mater 3:12269–12277

[26] Lee Y, Suntivich J, May KJ, Perry EE, Shao-Horn Y (2012) Synthesis and activities of rutile IrO_2 and RuO_2 nanoparticles for oxygen evolution in acid and alkaline solutions. J Phys Chem Lett 3:399–404

[27] Kuo D-Y, Paik H, Nelson JN, Shen KM, Schlom DG, Suntivich J (2019) Chlorine evolution reaction electrocatalysis on $RuO_2(110)$ and $IrO_2(110)$ grown using molecular-beam epitaxy. J Chem Phys 150:041726

[28] Walker J, Bruce King R, Tannenbaum R (2007) Sol–gel synthesis of hydrous ruthenium oxide nanonetworks from 1,2-epoxides. J Solid State Chem 180:2290–2297

[29] Bi R-R, Wu X-L, Cao F-F, Jiang L-Y, Guo Y-G, Wan L-J (2010) Highly dispersed RuO_2 nanoparticles on carbon nanotubes: facile synthesis and enhanced supercapacitance performance. J Phys Chem C 114:2448–2451

[30] Chang K-H, Hu C-C (2004) Hydrothermal synthesis of hydrous crystalline RuO_2 nanoparticles for supercapacitors. Electrochem Solid-State Lett 7:A466

[31] Vijayabala V, Senthilkumar N, Nehru K, Karvembu R (2018) Hydrothermal synthesis and characterization of ruthenium oxide nanosheets using polymer additive for supercapacitor applications. J Mater Sci Mater Electron 29:323–330

[32] Lin N, Tian J, Shan Z, Chen K, Liao W (2013) Hydrothermal synthesis of hydrous ruthenium oxide/graphene sheets for high-performance supercapacitors. Electrochim Acta 99:219–224

[33] Zhu K, Požgan F, D'Souza L, Richards RM (2006) Ionic liquid templated high surface area mesoporous silica and Ru–SiO_2. Microporous Mesoporous Mater 91:40–46

[34] Ma J, Chang L, Lian J, Huang Z, Duan X, Liu X, Peng P, Kim T, Liu Z, Zheng W (2010) Ionic liquid-modulated synthesis of ferrimagnetic Fe_3S_4 hierarchical superstructures. Chem Commun 46:5006–5008

[35] Manjunath K, Reddy Yadav LS, Jayalakshmi T, Reddy V, Rajanaika H, Nagaraju G (2018) Ionic liquid assisted hydrothermal synthesis of TiO_2 nanoparticles: photocatalytic and antibacterial activity. J Mater Res Technol 7:7–13

[36] Patterson AL (1939) The Scherrer formula for X-ray particle size determination. Phys Rev 56:978–982

[37] Bindu P, Thomas S (2014) Estimation of lattice strain in ZnO nanoparticles: X-ray peak profile analysis. J Theor Appl Phys 8:123–134

[38] Xu JH, Jarlborg T, Freeman AJ (1989) Self-consistent band structure of the rutile dioxides NbO_2, RuO_2, and IrO_2. Phys Rev B 40:7939–7947

[39] Cheng Z, Xu J, Zhong H, Chu X, Song J (2011) Hydrogen peroxide-assisted hydrothermal synthesis of hierarchical CuO flower-like nanostructures. Mater Lett 65:2047–2050

[40] Dziubinska-Kühn K, Croese J, Pupier M, Matysik J, Viger-Gravel J, Karg B, Kowalska M (2021) Structural analysis of water in ionic liquid domains—a low pressure study. J Mol Liq 334:116447

[41] Kim Y-T, Tadai K, Mitani T (2005) Highly dispersed ruthenium oxide nanoparticles on carboxylated carbon nanotubes for supercapacitor electrode materials. J Mater Chem 15:4914–4921

[42] Chen YM, Korotcov A, Hsu HP, Huang YS, Tsai DS (2007) Raman scattering characterization of well-aligned RuO_2 nanocrystals grown on sapphire substrates. New J Phys 9:130–130

[43] Chang K-H, Hu C-C, Chou C-Y (2007) Textural and capacitive characteristics of hydrothermally derived $RuO_{2\cdot}xH_2O$ nanocrystallites: independent control of crystal size and water content. Chem Mater 19:2112–2119

[44] Devadas A, Baranton S, Napporn TW, Coutanceau C (2011) Tailoring of RuO_2 nanoparticles by microwave assisted "Instant method" for energy storage applications. J Power Sources 196:4044–4053

[45] Liang Y-Y, Li HL, Zhang X-G (2007) Solid state synthesis of hydrous ruthenium oxide for supercapacitors. J Power Sources 173:599–605

[46] Amir FZ, Pham VH, Dickerson JH (2015) Facile synthesis of ultra-small ruthenium oxide nanoparticles anchored on reduced graphene oxide nanosheets for high-performance supercapacitors. RSC Adv 5:67638–67645

[47] Yang KS, Kim B-H (2015) Highly conductive, porous RuO_2/activated carbon nanofiber composites containing graphene for electrochemical capacitor electrodes. Electrochim Acta 186:337–344

[48] Biswal M, Banerjee A, Deo M, Ogale S (2013) From dead leaves to high energy density supercapacitors. Energy Environ Sci 6:1249–1259

[49] McCrory CCL, Jung S, Peters JC, Jaramillo TF (2013) Benchmarking heterogeneous electrocatalysts for the oxygen evolution reaction. J Am Chem Soc 135:16977–16987

[50] Fang Y-H, Liu Z-P (2010) Mechanism and Tafel lines of electro-oxidation of water to oxygen on $RuO_2(110)$. J Am Chem Soc 132:18214–18222

[51] Karlsson RKB, Cornell A (2016) Selectivity between oxygen and chlorine evolution in the chlor-alkali and chlorate processes. Chem Rev 116:2982–3028

[52] Arikado T, Iwakura C, Tamura H (1978) Some oxide catalysts for the anodic evolution of chlorine: reaction mechanism and catalytic activity. Electrochim Acta 23:9–15

[53] Trasatti S (1987) Progress in the understanding of the mechanism of chlorine evolution at oxide electrodes. Electrochim Acta 32:369–382

[54] Ma Z, Zhang Y, Liu S, Xu W, Wu L, Hsieh Y-C, Liu P, Zhu Y, Sasaki K, Renner JN, Ayers KE, Adzic RR (2018) Reaction mechanism for oxygen evolution on RuO_2, IrO_2, and $RuO_2@IrO_2$ core-shell nanocatalysts. J Electroanal Chem 819:296–305

[55] Trasatti S (2000) Electrocatalysis: understanding the success of DSA®. Electrochim Acta 45:2377–2385

Publisher's Note Springer Nature remains neutral with regard to jurisdictional claims in published maps and institutional affiliations.